Assimilating Copernicus SST Data into a Pan-Arctic Ice–Ocean Coupled Model with a Local SEIK Filter

XI LIANG,[a] QINGHUA YANG,[a] LARS NERGER,[b] SVETLANA N. LOSA,[b] BIAO ZHAO,[c] FEI ZHENG,[d] LIN ZHANG,[a] AND LIXIN WU[e,f]

[a] *Key Laboratory of Research on Marine Hazards Forecasting, National Marine Environmental Forecasting Center, Beijing, China*
[b] *Alfred Wegener Institute, Helmholtz Centre for Polar and Marine Research, Bremerhaven, Germany*
[c] *First Institute of Oceanography, State Oceanic Administration, Qingdao, China*
[d] *International Center for Climate and Environment Sciences, Institute of Atmospheric Physics, Chinese Academy of Sciences, Beijing, China*
[e] *Physical Oceanography Laboratory, Qingdao Collaborative Innovation Center of Marine Science and Technology (CIMST), Ocean University of China, Qingdao, China*
[f] *Qingdao National Laboratory for Marine Science and Technology, Qingdao, China*

(Manuscript received 24 August 2016, in final form 23 June 2017)

ABSTRACT

Sea surface temperature (SST) data from the Copernicus Marine Environment Monitoring Service are assimilated into a pan-Arctic ice–ocean coupled model using the ensemble-based local singular evolutive interpolated Kalman (LSEIK) filter. This study found that the SST deviation between model hindcasts and independent SST observations is reduced by the assimilation. Compared with model results without data assimilation, the deviation between the model hindcasts and independent SST observations has decreased by up to 0.2°C at the end of summer. The strongest SST improvements are located in the Greenland Sea, the Beaufort Sea, and the Canadian Arctic Archipelago. The SST assimilation also changes the sea ice concentration (SIC). Improvements of the ice concentrations are found in the Canadian Arctic Archipelago, the Beaufort Sea, and the central Arctic basin, while negative effects occur in the west area of the eastern Siberian Sea and the Laptev Sea. Also, sea ice thickness (SIT) benefits from ensemble SST assimilation. A comparison with upward-looking sonar observations reveals that hindcasts of SIT are improved in the Beaufort Sea by assimilating reliable SST observations into light ice areas. This study illustrates the advantages of assimilating SST observations into an ice–ocean coupled model system and suggests that SST assimilation can improve SIT hindcasts regionally during the melting season.

1. Introduction

The Arctic climate has undergone a rapid change during the last 30 years. The observed summer sea ice extent decreased at a rate of 13% decade^{-1} from 1979 to 2014. In 2012 the new record September Arctic minimum sea ice extent appeared, in which the ice extent reduced by 49% relative to the 1979–2000 September climatology (Overland and Wang 2013). Along with evidence of the reduction in sea ice extent, sea ice drilling observations also revealed a large decline in the thickness of multiyear sea ice, even though ice thickness measurements are difficult to take. The intense thickness decline of multiyear sea ice was observed over the last 9 years (Overland and Wang 2013). As the summer sea ice retreats, the Arctic Ocean is providing new opportunities for scientific research and commercial navigation. The Arctic marine environmental forecasts (sea ice, ocean and atmosphere) are therefore urgently needed to well manage the opportunities (Jung et al. 2016).

As an essential part to reduce the uncertainties associated with the initial states and external forcing, data assimilation methods have been widely involved in forecasting systems to improve forecasting accuracy. Many studies have shown the advantages of assimilating ocean data into ocean models to improve the ocean prediction skills (Brusdal et al. 2003; Brasseur et al. 2005; Stanev et al. 2011). Brusdal et al. (2003) assimilated

Corresponding author: Xi Liang, liangx@nmefc.gov.cn

DOI: 10.1175/JTECH-D-16-0166.1

sea level anomaly (SLA) and SST data into a nonlinear Miami Isopycnic Coordinate Ocean Model in the North Atlantic by using three ensemble Kalman filters. They found that all the hindcasts of sea level anomaly, SST, sea salinity fields, subsurface temperature, the thickness of the isopycnic layers, and velocity fields were improved. Using the singular extended evolutive Kalman (Brasseur et al. 1998) filter analysis method, a multivariate set of observations (along-track altimetry, in situ temperature, salinity profile data, and SSTs) was assimilated into a first prototype eddy-permitting North Atlantic configuration of the Nucleus for European Modelling of the Ocean (Madec et al. 1998) primitive equation model. The assimilation resulted in an improvement of the temperature at all depths, thermocline, and annual mean surface current, especially in the Gulf of Mexico and the Caribbean Sea (Brasseur et al. 2005). Stanev et al. (2011) assimilated surface current and SST data from stationary stations, a high-frequency radar system, a FerryBox system (Petersen et al. 2011), and satellites into a 3D hydrodynamic model in the coastal area of the German Bight. The assimilation substantially improved modeled SST, sea surface salinity, and surface current fields not only in the vicinity of the ferry track but also over larger model areas.

Other studies also have shown the advantages of assimilating ice data into ice–ocean models to improve the ice prediction capabilities (Lisæter et al. 2003, 2007; Tietsche et al. 2013; Yang et al. 2014, 2015). Lisæter et al. (2003) assimilated ice concentration data into a coupled ice–ocean model by ensemble Kalman filter (EnKF; Evensen 1994); it was found that ice concentration improvements appeared in the ice edge areas in summer. Lisæter et al. (2007) assimilated *CryoSat* ice thickness measurements into a coupled Arctic ice–ocean model with the EnKF. The results show that surface properties of the ocean, such as ocean salinity, surface temperature, and ice concentration fields, can benefit from the ice thickness assimilation if reasonably configured stochastic wind forcing is used. Tietsche et al. (2013) illustrated that assimilation of ice concentration can improve the ice thickness simulation in a global climate model. Yang et al. (2015) assimilated summer sea ice concentration (SIC) data into a coupled ice–ocean model with the local singular evolutive interpolated Kalman (LSEIK) filter. The assimilation resulted in an improvement of the sea ice edge, concentration, and thickness forecasts.

However, only a few studies investigated the influence of assimilating ocean data on the coupled ice–ocean model system, especially the simulation of sea ice. A multivariate set of observations (SLA, SST, in situ temperature and salinity, ice concentration, ice drift) was assimilated into the Norwegian Tunable Optical Profiler for Aerosol and Ozone (TOPAZ) forecasting system (Sakov et al. 2012). Noticeable improvements were found for ice extents, ice thickness, salinity in the Arctic, and temperature in the Fram Strait, but the paper did not examine the effects of ocean data assimilation on the simulation of sea ice.

To forecast the Arctic Ocean environment, aiming at an operational implementation of a reliable ice–ocean forecasting system, a pan-Arctic ice–ocean coupled model system was established two years ago at the National Marine Environmental Forecasting Center. The system is based on the Regional Ocean Modeling System (ROMS; Shchepetkin and McWilliams 2003, 2005; Moore et al. 2004) but does not include a data assimilation module. Recently, a data assimilation module based on the Parallel Data Assimilation Framework (PDAF; Nerger and Hiller 2013) using the ensemble-based local SEIK filter was developed for the pan-Arctic ice–ocean coupled model system. Here we report on the assimilation of satellite SST observations into the pan-Arctic ice–ocean model system in a hindcast mode for the period of May–September 2014. An ensemble of only four members is used. The analysis of the assimilation experiment shows that, despite the very small ensemble size, a substantial improvement of the modeled SST can be obtained. The effects of the SST assimilation on ice concentration and thickness will be presented in our study.

The rest of this paper is organized as follows. Section 2 provides a description of the model configuration, the data assimilation, and the experiment design. In section 3 we will assess the model results without and with data assimilation. A summary and conclusions will be given in section 4.

2. Model configuration, data assimilation, and experiment design

a. Pan-Arctic ice–ocean coupled model

The Arctic ice–ocean coupled model system is based on ROMS. ROMS is a widely used, free-surface, terrain-following primitive equation ocean model that was originally developed at Rutgers University. ROMS has special advantages for regional- and basin-scale ocean modeling (Marchesiello et al. 2003; Di Lorenzo 2003; Budgell 2005). ROMS includes the four separate dynamic kernels, which are nonlinear, tangent linear, representer tangent linear, and adjoint. Shchepetkin and McWilliams (2003, 2005) described the algorithms of the ROMS nonlinear kernel in detail, while Moore et al. (2004) presented the algorithms of the tangent linear and adjoint kernels. ROMS also includes several coupled

model components for biogeochemical, sediment, biological, and sea ice simulations. The sea ice component of ROMS is a combination of the elastic–viscous–plastic (EVP) rheology (Hunke and Dukowicz 1997; Hunke 2001) and simple one-layer ice and snow thermodynamics with a molecular sublayer under the ice (Mellor and Kantha 1989). The dynamics and thermodynamics of the coupled sea ice component are described in Budgell (2005).

In our application, the Arctic ice–ocean coupled model system uses the nonlinear kernel and the sea ice model component of ROMS. For the Arctic model configuration, polar stereographic coordinates are used. The nonlinear kernel and the sea ice model have the same horizontal grids with 1159 × 999 grid points, a maximum grid distance of 6.22 km, and a minimum grid distance of 4.23 km. The system uses 30 vertical layers of the nonlinear kernel with stretched terrain-following coordinates (Song and Haidvogel 1994). The topographical data are from International Bathymetric Chart of the Arctic Ocean, version 2.23, which has a horizontal resolution of 2 km and was interpolated onto the model grid (Fig. 1). The Mellor–Yamada level 2.5 parameterization (Mellor and Yamada 1982) is chosen as the vertical mixing scheme, although *K*-profile (Large et al. 1994) and generic length scale parameterizations (Umlauf and Burchard 2003) are optional.

The initial ocean fields are extracted from the 1988–2007 averaged annual mean value of the Simple Ocean Data Assimilation, version 2.2.0 (SODA 2.2.0; Giese and Ray 2011). The ocean open boundary condition is extracted from the 1988–2007 averaged monthly mean value of SODA 2.2.0. The atmospheric external forcing, which is used to spin up the model, is extracted from the 1994–2013 averaged monthly mean value of the National Centers for Environmental Prediction Reanalysis-2 (NCEP–DOE AMIP-II Reanalysis; Kanamitsu et al. 2002). From 1 January 2014 on, the model is forced by the 0.5°-resolution daily atmospheric forecast forcing data from the Global Forecast System (GFS; Kanamitsu 1989) to ensure more realistic atmospheric forecast forcing during the data assimilation experiment. The runoff data of six large rivers in the Arctic come from the monthly mean value of the Arctic Great Rivers Observatory (Peterson et al. 2002) dataset.

The initial SIC field is from the 25-km Special Sensor Microwave Imager (SSM/I) *F15* dataset (Wentz and Meissner 2000). SSM/I *F-15* is a near-polar-orbiting passive microwave radiometer that has been carried onboard the Defense Meteorological Satellite Program satellite since December 1999. The initial sea ice thickness (SIT) field is from the Global Ice–Ocean Modeling and Assimilation System dataset (Zhang and Rothrock 2003). The landfast ice is initialized with data from the National Snow and Ice Data Center (Konig Beatty 2012).

b. *Ensemble data assimilation*

In ensemble data assimilation methods, an ensemble of model state realizations is used to represent possible model evolution trajectories, which include the uncertainty of the model state. This uncertainty can be due to different errors, for example, generated by inaccurate observations, coarse external forcing, and relatively simple parameterizations. All ensemble states are integrated by the model in the so-called forecast phase. These forecasts then represent a statistical sampling of the uncertainty in the forecast model state. The ensemble mean and ensemble covariance matrix are then used in the analysis step where the observations are assimilated. The statistics of the ensemble are diagnosed to verify the assimilation reliability (Candille et al. 2007; Rodwell et al. 2016). The computing cost of the data assimilation process is usually determined by the cost of integrating the ensemble states using the model. Thus, while increasing the ensemble size will improve the error estimates, it will also enlarge the computing cost and thus lead to decreasing forecast efficiency. In practice only ensembles of order 10–100 are feasible to compute.

To allow for a stable data assimilation process with ensembles that are very small compared to the number of grid points in a model, a localization of the filter analysis is used. The localization is obtained by separately updating each single water column using only observations within a specified influence radius around each water column. In addition, the observational influence is weighted according to the distance of an observation from the surface grid point that is updated (see, e.g., Losa et al. 2012, 2014).

In this study, the LSEIK filter (Nerger et al. 2006) as implemented in PDAF (http://pdaf.awi.de; Nerger and Hiller 2013) is used. PDAF is a software environment for ensemble data assimilation that was developed at the Alfred Wegener Institute in Germany. It contains fully implemented and optimized data assimilation algorithms, in particular ensemble-based Kalman filters. For the data assimilation, a state vector is defined that is composed of SST, SIC, and SIT. Thus, only these three variables are directly modified in the analysis step. During the following forecast phase, other model variables will react dynamically to the changes in the variables contained in the state vector.

The data assimilation experiment begins 1 May 2014 with an ensemble of four model states generated from second-order exact sampling (Pham 2001) from a model trajectory. For this procedure, daily snapshots for the

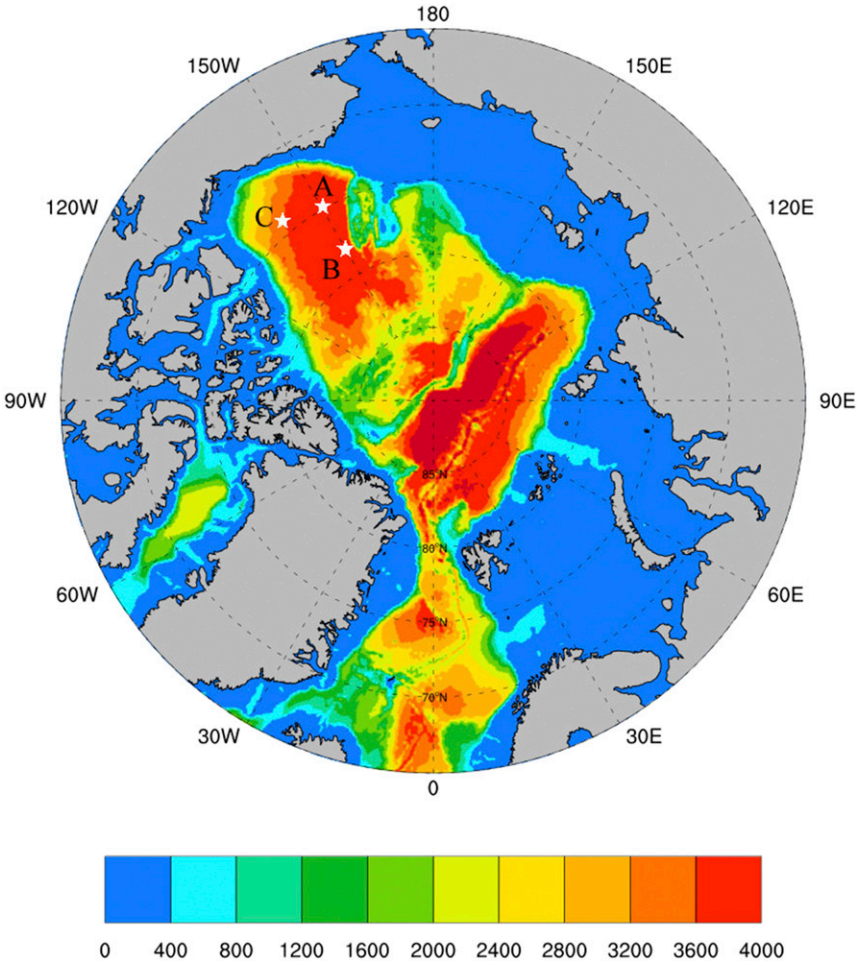

FIG. 1. Topography of the model domain (m) and position of the BGEP ULS: A: BGEP_uls13a (74.99°N, 149.98°W), B: BGEP_uls13b (77.99°N, 150.06°W), and C: BGEP_uls13c (73.99°N, 139.95°W).

three model variables (SST, SIC, SIT) are stored as columns of a matrix for the period 1 May–31 July 2014 from the experiment without data assimilation. After subtracting the mean of these states, a singular value decomposition is computed. The leading four modes of the singular value decomposition are then used to generate ensemble members of the initial fields by multiplying them with a random matrix that preserves the mean and covariance contained in the models. With this ensemble generation method, the ensemble members represent possible ocean states, the ensemble mean represents the best estimate, and the ensemble spread represents the uncertainty that arises from model variability.

At the initial time and after each ensemble forecast of 24 h, an analysis step is computed in which the ensemble members are used to assimilate the observational SST data with the LSEIK filter to generate new ensemble members. On each model grid point, the localization radius is set to 12 grid points, corresponding to approximately 50 km. Within the localization radius, all observations are weighted exponentially according to their distance to the analyzed grid point.

In the ensemble forecasts, each ensemble member is integrated over 24 h using ROMS driven by all forcings, such as atmospheric forcing, ocean open boundary condition, and river runoff.

c. *Observational data*

The SST observations, which are assimilated, are from the Arctic Ocean High Resolution Sea Surface Temperature Analysis from the Copernicus Marine Environment Monitoring Service (product SST_ARC_SST_L4_NRT_OBSERVATIONS_010_008_b, available from http://marine.copernicus.eu). The dataset provides near-real-time daily satellite gap-free Level-4 sea surface temperature. The SST data are derived from infrared and microwave radiometers, and have a horizontal resolution

of 0.03° × 0.03°. The dataset also provides estimated error standard deviations of the SST. It is a state-of-the-art Arctic SST product for operational implementation. For the experiment performed here, the SST observations are interpolated onto the model grid. For the data assimilation, the error of the SST data is approximated as a constant error of 0.7°C. This error estimate contains not only the measurement error but also representation errors, for example, as a result of the different resolutions of the data product and the model grid.

For the validation of the experiments, independent SST data from the Real-Time Global Sea Surface Temperature High-Resolution (RTG_SST_HR) analysis from the Marine Modeling and Analysis Branch in NCEP (available from ftp://polar.ncep.noaa.gov/pub/sst/rtg_high_res) are used. The daily RTG_SST_HR product is produced on a 0.083° × 0.083° grid with a two-dimensional variational interpolation analysis of the most recent 24 h of buoy and ship data, satellite-retrieved SST data, and SST derived from the satellite-observed sea ice coverage. The Arctic section of RTG_SST_HR data are extracted and used for comparison in our experiment.

To evaluate the effect of the data assimilation on the SIC, observations of SIC from the near-real-time daily Advanced Microwave Scanning Radiometer 2 (AMSR2) provided by the Institute of Environmental Physics, University of Bremen (available from http://www.iup.uni-bremen.de:8084/amsr2data/asi_daygrid_swath/n6250/), are used. The AMSR2 on board the *Global Change Observation Mission–Water* satellite was launched on 18 May 2012 and daily SIC maps are available from 26 January 2013.

The effect of the data assimilation on the SIT is assessed using SIT observations at three positions in the Beaufort Gyre (BG) from the Beaufort Gyre Exploration Project (BGEP). The thickness is measured by an upward-looking sonar (ULS) that is mounted in the uppermost mooring floatation. The ULS samples the ice draft with a precision of ±0.3 m in ice thickness. Drafts are converted to thickness by multiplying a factor of 1.1 (Nguyen et al. 2011). Data from three moorings are used whose locations are shown in Fig. 1: BGEP_uls13a is moored at 74.99°N, 149.98°W to sample ice thickness from 14 August 2013 to 30 September 2014 with a sampling interval of 2 s; BGEP_uls13b is moored at 77.99°N, 150.06°W to sample ice thickness from 21 August 2013 to 7 October 2014; and BGEP_uls13c is moored at 73.99°N, 139.95°W to sample ice draft from 9 August 2013 to 26 September 2014. Daily SIT data from the three ULSs are used in the experiments to validate the SIT (the data are available from the BGEP website, http://www.whoi.edu/website/beaufortgyre/data).

d. *Experiment design*

A schematic of the experiment design is shown in Fig. 2. From the initial ocean field, the pan-Arctic ice–ocean coupled model system has been integrated for 20 model years forced by NCEP–DOE AMIP-II Reanalysis atmospheric data. After this spinup period, the system reaches a relatively stable state. Starting on 1 January 2014, the monthly NCEP–DOE AMIP-II Reanalysis atmospheric forcing is replaced by GFS daily atmospheric forcing. The simulation is then continued until 30 September 2014. This hindcast experiment without data assimilation is referred to as Ex_NoDA.

Ex_EnDA begins on 1 May 2014. Starting from the initial ensemble, alternating analysis steps and 24-h ensemble forecasts are performed every day until 30 Sep 2014.

The simulation results of the two experiments are analyzed for the period from 1 May to 30 September 2014 with the independent SST, AMSR2 SIC, and BGEP SIT data to discuss the effect of the SST assimilation on the Arctic model hindcasts.

3. Results

a. *SST*

To assess the experiments, the model fields at three dates—20 June, 10 August, and 30 September 2014, thus after the spin up of the data assimilation process—are examined. Figure 3 shows the modeled SST and the absolute value of the deviation between the modeled SST and independent NCEP SST data on 20 June 2014. The SST deviation in heavy ice-covered areas with AMSR2 SIC larger than 80% is not shown in the figure because satellite-retrieved SST data have large errors in these areas. In Ex_NoDA, the SST deviates from the NCEP SST data by about 5°C in the northern coastal regions of the European–Asian continent. Another large deviation of up to 4°C is visible along the eastern coast of Greenland. The large deviations close to the coasts of more than 4°–5°C result from when the model grid is covered by sea ice but the observation is in open water. In the Greenland Sea, the SST deviation in the western basin is larger than that in the eastern basin. In the Barents Sea, the SST deviation is generally larger than 1.5°C with a maximum of 3.5°C. Over the whole model domain, the root-mean-square error (RMSE) between the SST from Ex_NoDA and NCEP SST data is 2.31°C (Fig. 3a). With the data assimilation in Ex_EnDA, the cycling of forecasts and analyses improves the modeled SST field. In the ensemble forecast on 20 June

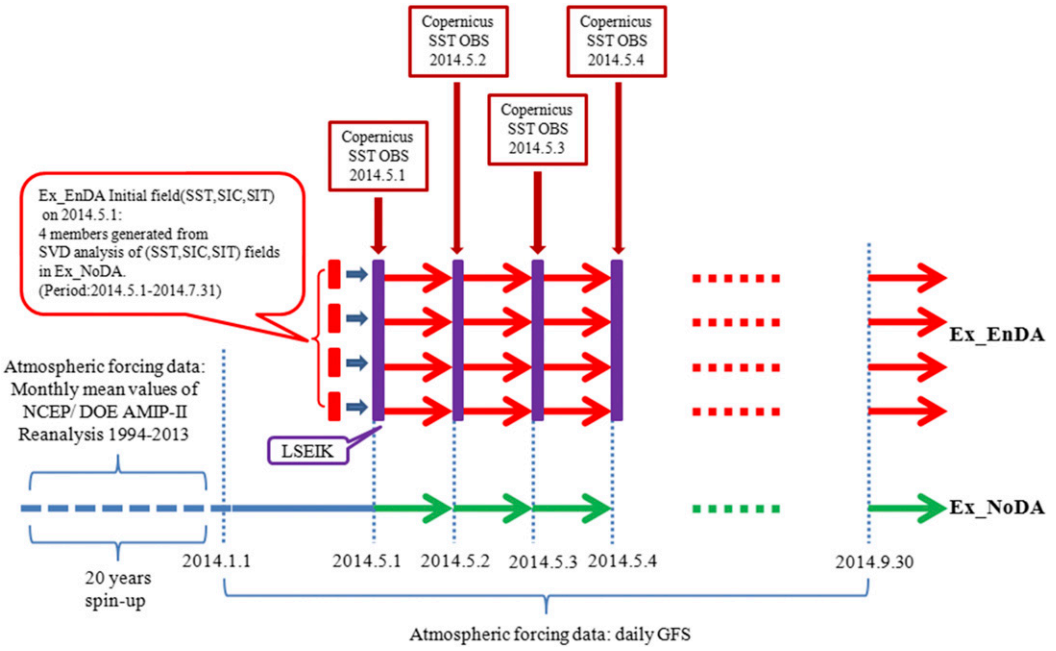

FIG. 2. Schematic of the experiments.

2014, the RMSE is reduced by 0.05°C (Fig. 3b). The LSEIK analysis step further corrects the SST field, reducing the RMSE between the SST analysis field and the NCEP SST data by another 0.06°C (Fig. 3c). The difference in the deviation plots from Ex_NoDA and Ex_EnDA in Fig. 3d shows the improvement of the SST field as a result of the data assimilation. Positive values depict an improvement, while negative values show that the SST is deteriorated. The data assimilation improves the SST by up to 0.5°C in the central areas of the Greenland Sea. In other sectors of the Arctic Ocean, SST is also improved by more than 2°C. However, there are also regions where the data assimilation deteriorates the SST, such as south of Svalbard, at the eastern edge of the ice on the east coast of Greenland, and in the northern part of Baffin Bay.

Figure 4 shows the modeled SST and the absolute deviation of SST on 10 August 2014. Compared to 20 June, the area with SICs of less than 80% has significantly increased. The RMSE in the modeled SST from Ex_NoDA has increased to 2.84°C in the middle of the summer. Figure 4a shows that SST deviations of more than 4°C appear in the Chukchi Sea, the western East Siberian Sea, the Laptev Sea, the central Barents Sea, and the western Greenland Sea. The deviation in the Pacific sector is generally larger than that in the Atlantic sector. Compared to Ex_NoDA, the data assimilation reduces the RMSE in the 24-h forecasts by 0.06°C (Fig. 4b) and the analysis by 0.1°C (Fig. 4c). The largest SST improvements appear in the northern Greenland Sea and the Beaufort Sea (Fig. 4d). Deteriorations of the SST field are still visible in Baffin Bay and the region south of Svalbard.

Figure 5 shows the modeled SST and the absolute SST deviation on 30 September 2014. The errors in the SST field of Ex_NoDA shrink at the end of the summer, and the RMSE is reduced to 2.04°C. Deviations of more than 3°C appear now in the Beaufort Sea, the central East Siberian Sea, and the southern Barents Sea (Fig. 5a). Because of the ensemble data assimilation, the SST RMSE is reduced by 0.06°C in the forecast field (Fig. 5b), while the SST analysis reduces the RMSE by 0.13°C (Fig. 5c). The largest SST improvements appear in the Beaufort Sea and the eastern Greenland Sea (Fig. 5d). At this time only small deteriorations of the SST are visible. They are mainly located in Baffin Bay, while the deterioration south of Svalbard is significantly reduced compared to the earlier dates.

Figure 6 compares the time evolution of RMSE between NCEP SST data and the modeled SST with and without data assimilation. The RMSEs are averaged over the full model domain excluding the areas with SIC larger than 80%. The SST from Ex_NoDA shows a large deviation from the NCEP SST data in the middle of summer, reaching a maximum of 3.4°C around 19 July 2014. The deviation is smaller in spring and in late summer. The minimum RMSE of 1.7°C appears

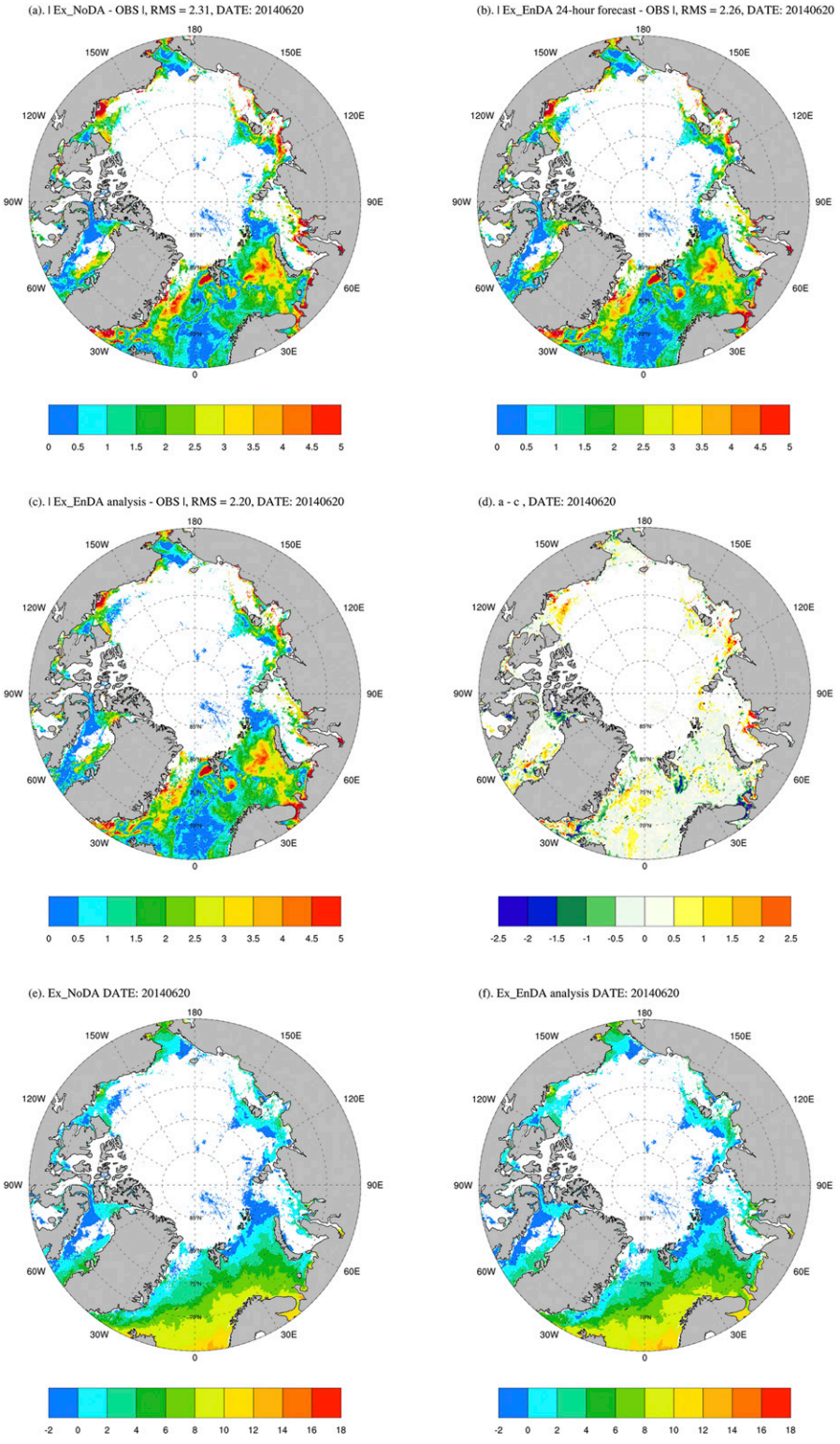

FIG. 3. Absolute deviation (°C) between modeled SST and NCEP SST data: (a) Ex_NoDA, (b) Ex_EnDA24-h forecast, (c) Ex_EnDA analysis, (d) Data assimilation improvement [(a) minus (c)]. Modeled SST (°C): (e) Ex_NoDA and (f) Ex_EnDA analysis on 20 Jun 2014. Coverage of the heavy ice cover with AMSR2 SIC larger than 80% is reduced, giving more space to see the data assimilation influence.

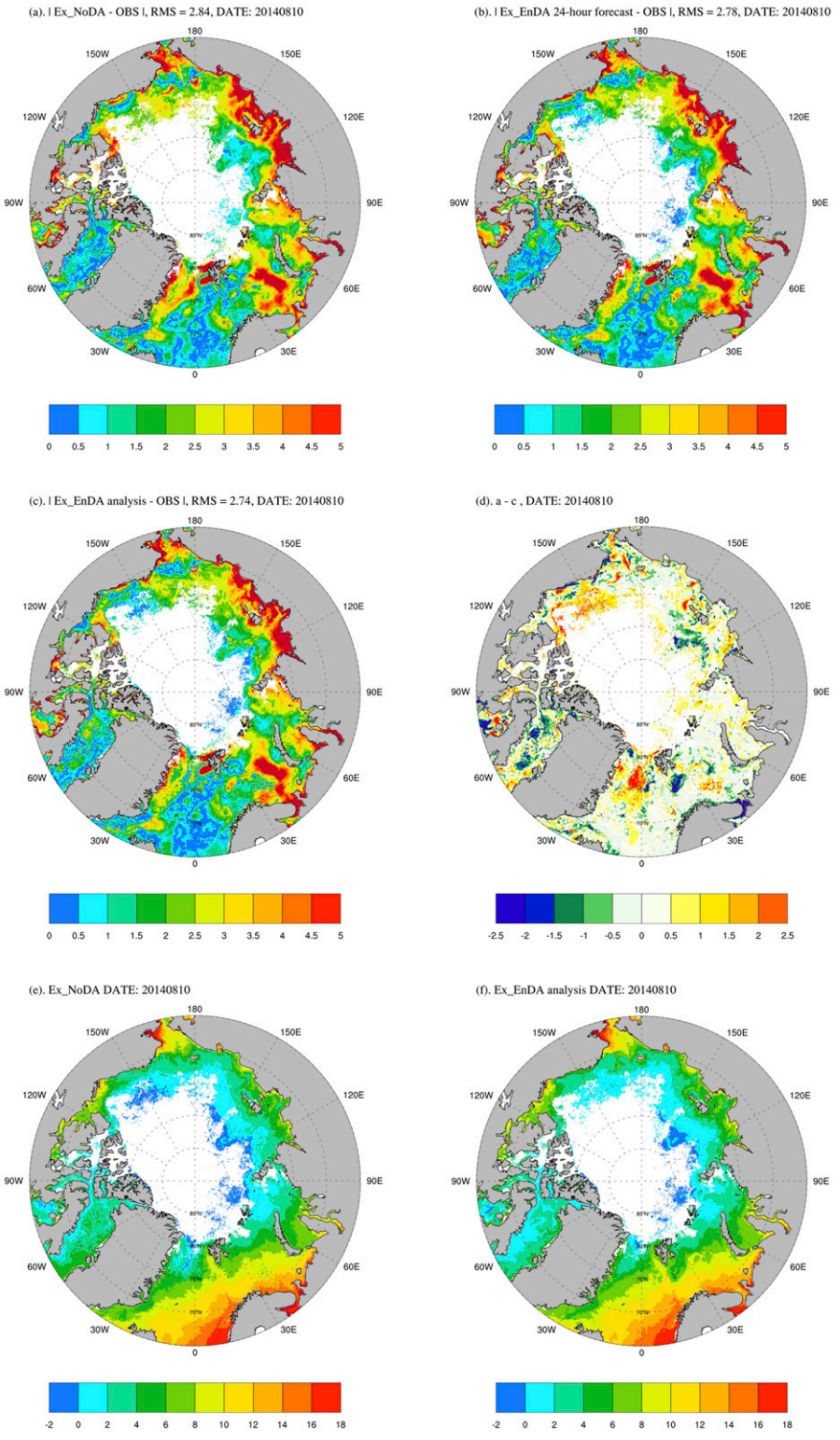

FIG. 4. As in Fig. 3, but for 10 Aug 2014.

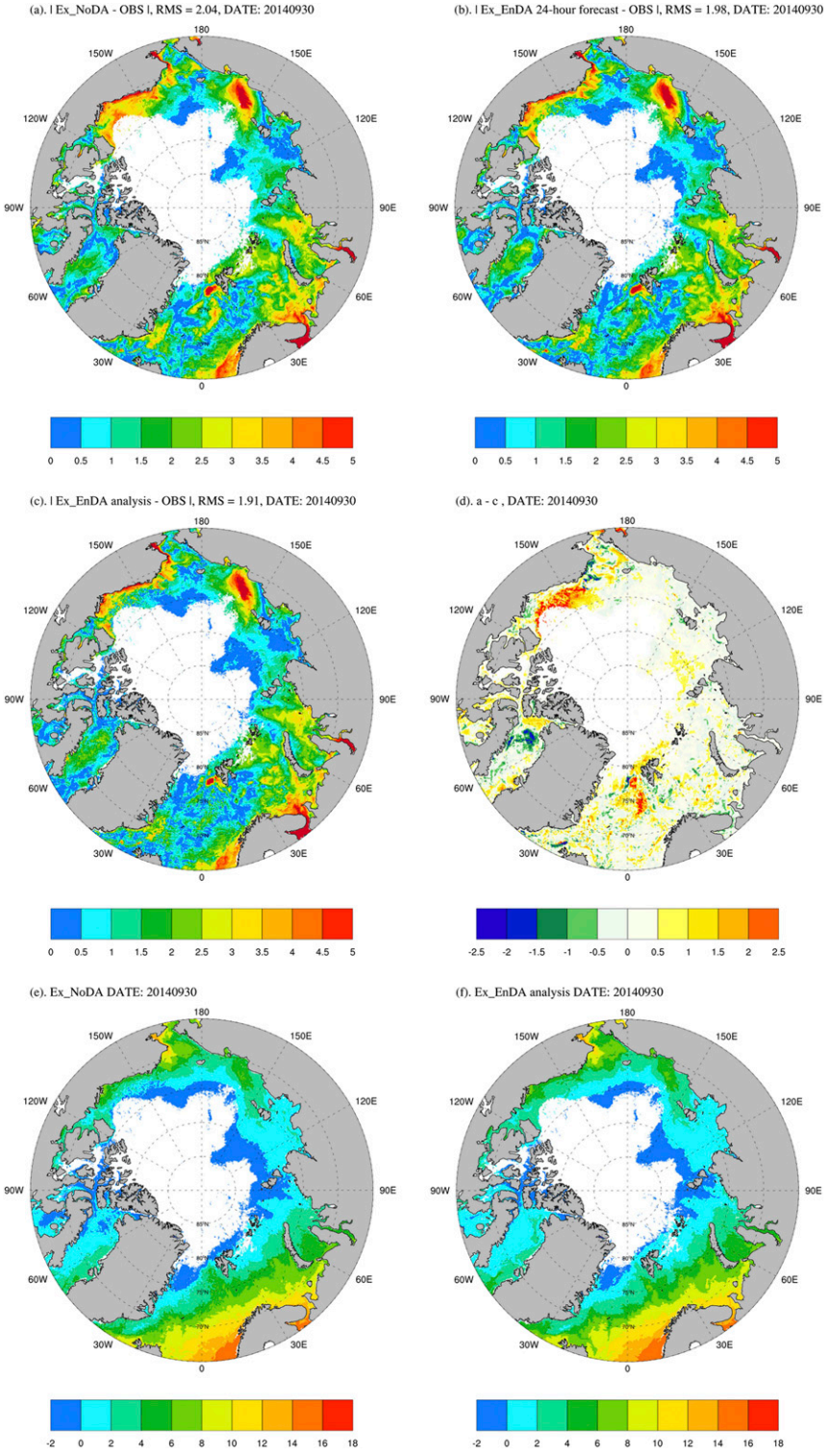

FIG. 5. As in Fig. 3, but for 30 Sep 2014.

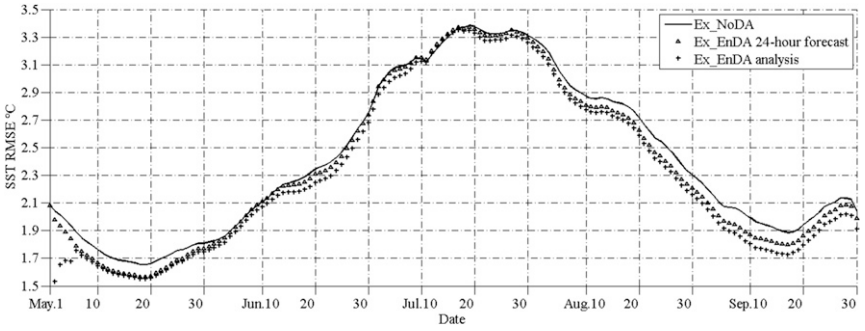

FIG. 6. Time evolution of RMSE between NCEP SST data (°C) and Ex_NoDA (line), Ex_EnDA24-h forecasts (triangle), and Ex_EnDA analysis (cross). Areas with AMSR2 SIC larger than 80% are not taken into account.

around 18 May 2014. The Ex_EnDA SST shows smaller deviations from the NCEP SST data than the Ex_NoDA SST. The RMSE difference of both experiments is smaller in the middle of the summer than in spring and late summer. The data assimilation reduces the RMSE by up to 0.2°C compared to Ex_NoDA. During each forecast phase, the error in the SST field increases but remains below the error of Ex_NoDA. At each analysis step, the data assimilation system merges the observational SST information into the model trajectory and reduces the RMSE.

Ex_EnDA begins at 1 May 2014, modeled SST is updated after assimilating the SST observations, and the differences between Ex_EnDA SST and Ex_NoDA SST on 1 May 2014 can be seen as a perturbation. During the following forecast step, this perturbation is suppressed by the energy from the subsurface layer. After 5 May 2014, Ex_EnDA reaches a dynamic balance between the SST assimilation effects and upper-ocean thermodynamics. The conflict trends before 5 May 2014 come from a spinup process as a result of suddenly assimilating SST into the model system.

b. Sea ice concentration

To assess the influence of the data assimilation on the SIC, the same three dates are chosen as for the SST. The SIC is updated by the data assimilation through the cross covariances between SST and SIC, which are estimated by the ensemble. The difference between the modeled SIC fields from AMSR2 observations are shown in Fig. 7. The first and second columns show the differences for Ex_noDA and Ex_DA, respectively. The third column shows the difference of the absolute values of the two first columns, which can be interpreted as the improvement by the assimilation. Thus, the assimilation reduced the deviation from the observation for positive values and negative values indicate deteriorations. Generally, the modeled SIC shows a wider sea ice extent than the AMSR2 sea ice observations on all three dates. This difference represents a model bias, which is visible as red areas in the difference plots in the left and middle columns of Fig. 7. This bias is only partially corrected by the data assimilation. The third column shows that, as another general feature, the changes by the data assimilation increase during the course of the assimilation experiment.

Figure 7a shows the difference between Ex_NoDA and the AMSR2 SIC observation on 20 June 2014. The model bias results in concentration deviations of more than 30% in the western Greenland Sea, the northern Barents Sea, the southern Kara Sea, the Laptev Sea, the Chukchi Sea, the southern Beaufort Sea, and Baffin Bay. At this date improvements in the SIC are visible only in small regions close to the coast (Figs. 7b and 7c) and the RMS deviation is reduced only from 28.76% to 28.56%. On 10 August 2014, Ex_NoDA again overestimates the sea ice extent. More than 30% SIC deviation appears around the central Arctic ice cap (Fig. 7d). The data assimilation improved the SIC in the Canadian Arctic Archipelago, but deteriorated it around the New Siberian Islands (Fig. 7f). Here, the ensemble estimates of the cross correlation between SST and SIC appear to be insufficient to correct the SIC based on the SST correction, so the spatially averaged RMS deviation is not reduced. On 30 September 2014, extended improvements as a result of the data assimilation in Ex_EnDA are visible around the edge of the Arctic ice cap. Remarkable SIC improvement is located in the southern Beaufort Sea and the northern Greenland Sea. The SIC of the heavy ice region in the central Beaufort Gyre is also improved (Figs. 7h and 7i). However, there are also regions in which the SIC is deteriorated in Ex_EnDA. Overall, the RMS deviation between the modeled and observed SIC is reduced from 21.68% to 21.09%.

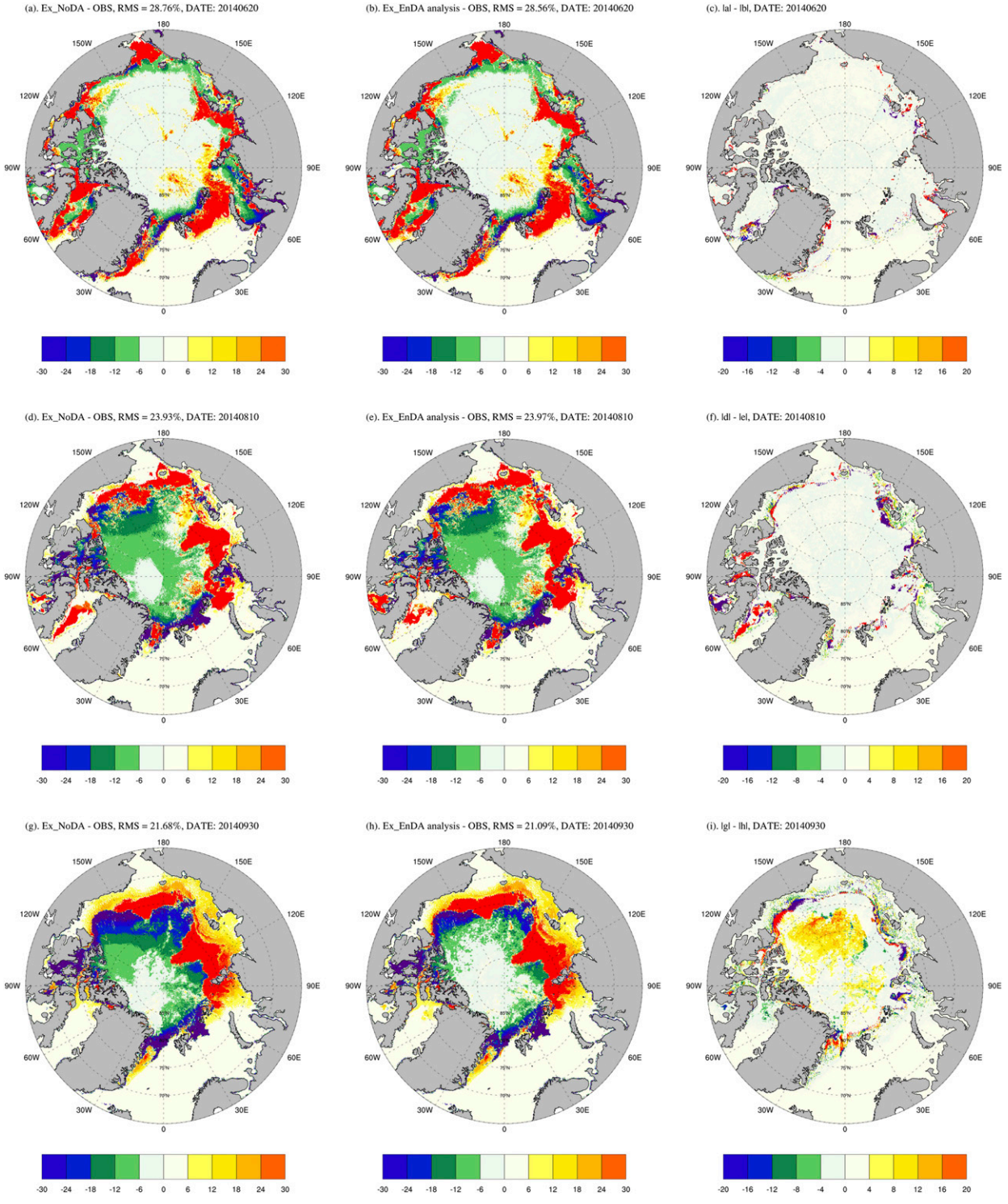

FIG. 7. Deviation (%) between modeled SIC and AMSR2 SIC data. (top) 20 Jun 2014, (middle) 10 Aug 2014, and (bottom) 30 Sep 2014. (left) Ex_NoDA, (center) Ex_EnDA analysis, (right) improvement (absolute difference: left column minus center column).

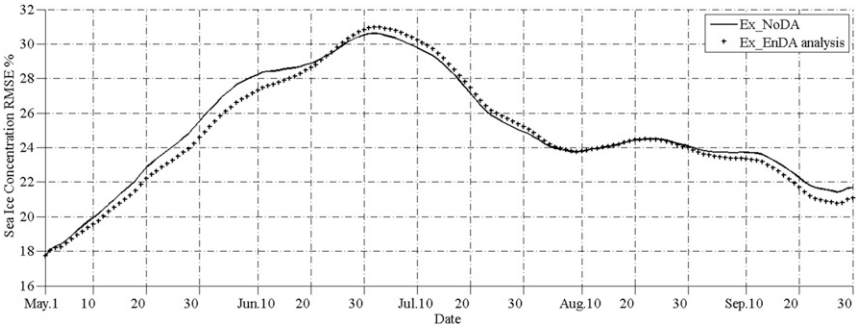

FIG. 8. Time evolution of RMSE (%) between AMSR2 SIC data and Ex_NoDA (line) and Ex_EnDA analysis (cross).

Figure 8 presents the time evolution of RMSE between the SIC data from AMSR2 and the model with and without data assimilation. Ex_NoDA shows a maximum SIC deviation of 31% from the AMSR2 observation around 30 June 2014. By assimilating SST observations, the SIC is improved before 24 June 2014, but then it is slightly deteriorated until 10 August 2014. Overall, the SIC improvement of the domain-averaged RMSE is not substantial in the Ex_EnDA experiment. This is partly due to the SIC bias in the model, which is not corrected by the data assimilation. The influence of the data assimilation is particularly small at the beginning of the experiment, while the changes in the SST are relatively large. This situation is related to the very small ensemble used in the data assimilation experiment. Because only SST data are assimilated, the SIC is changed by the data assimilation using the ensemble-estimated cross correlations between SST and SIC. Because of the very small ensemble, these cross correlations are small but also noisy, so the corrections at the analysis step of the data assimilation process are less systematic. As a second effect, the SIC reacts to the changed SST through the model dynamics in the forecast phases.

c. *Sea ice thickness*

Because of the technical difficulty of SIT satellite remote sensing, large-scale maps of SIT observations are currently not available, which especially concerns the summer season. However, on-site mooring data obtained from upward-looking sonar can give us some information about SIT at specific locations. Here, ice draft data from three ULSs at different positions in the Beaufort Sea are compared with the modeled SIT with and without data assimilation (Fig. 9).

The sea ice in the experiment Ex_NoDA at location A in Fig. 1 is thicker than that of the ULS observation. The difference is about 0.6 m in May and June and reaches a maximum of about 1.5 m on 10 August 2014. By assimilating the SST observations, the SIT is also improved. No obvious changes in the SIT appear before July. This is because the SIC is larger than 80% in the Beaufort Sea during May and June, so SST observations are not assimilated into the model fields of the Beaufort Sea. After 30 June 2014, the SIC is sufficiently small, so the data assimilation has an effect in this region; thus, the thickness from Ex_EnDA becomes gradually closer to the ULS observation compared to Ex_NoDA (Fig. 9a). A minimum deviation of about 0.1 m is reached at the end of the assimilation experiment. Similar effects of the data assimilation are obtained for the two other ULS time series (Figs. 9b and 9c). For location C, the thickness error is reduced to zero at the end of the data assimilation experiments. From Fig. 7, the model has significantly overestimated SIC in the south Beaufort Sea in relation to Figs. 4 and 5, the SST after assimilating the observations becomes warmer in this region, and the RMSE between the modeled SST and the observations reduced significantly, which means the cold bias can be constrained, so more warm water results in the sea ice melting faster. The thickness at location B is reduced less than at the position of the two other ULS measurements. This is likely due to the farther poleward location, so the data assimilation has a smaller influence compared to the two other positions.

4. Summary and conclusions

In this paper, satellite SST data are assimilated into a pan-Arctic ice–ocean coupled model by applying the ensemble-based LSEIK filter. The data assimilation reduces the deviation between the modeled SST and independent SST observations. Compared with model results without data assimilation, the root-mean-square error between modeled SST and independent SST observations has decreased by up to 0.2°C at the end of summer. Remarkable improvements in the SST are located in the Greenland Sea, the Beaufort Sea, and

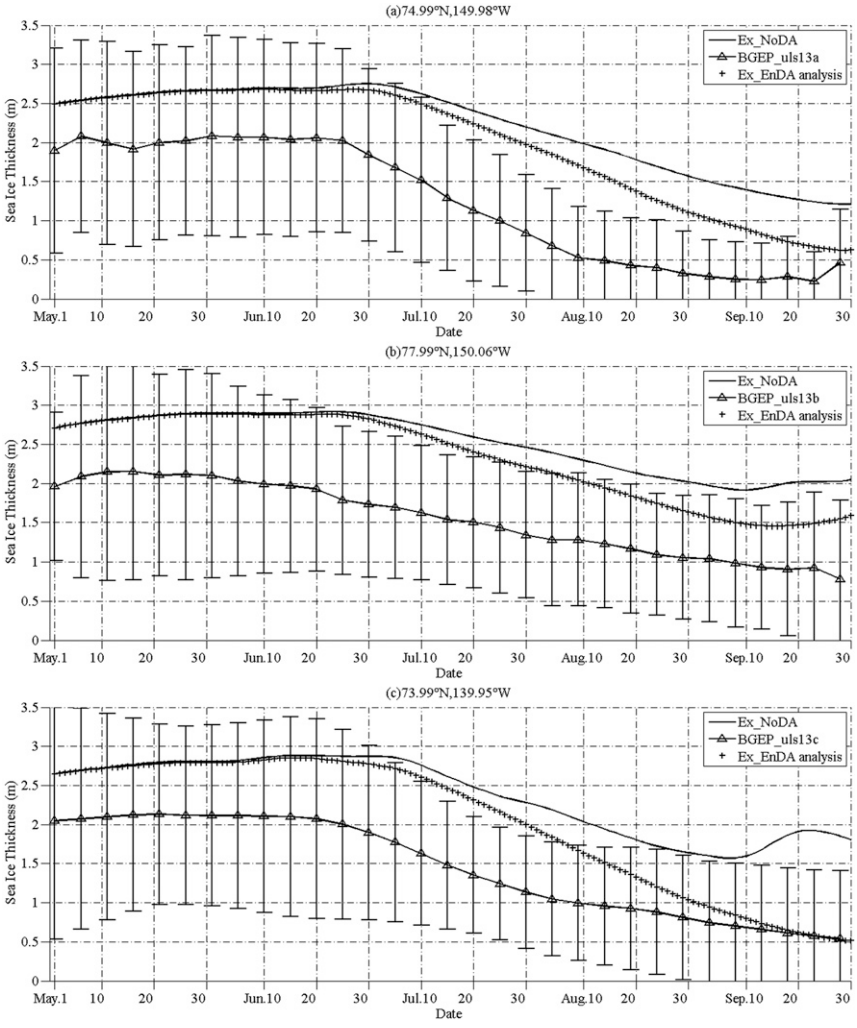

FIG. 9. Time evolution of SIT of Ex_NoDA (line), Ex_EnDA analysis (cross), and BGEP ULS observations (line with triangle) at three positions: (a) 74.99°N, 149.98°W; (b) 77.99°N, 150.06°W; and (c) 73.99°N, 139.95°W. Lines of BGEP ULS observations have been smoothed with bar representing the variability.

the Canadian Arctic Archipelago. The effects of SST assimilation on SIC are not straightforward. SICs are improved regionally in the Canadian Arctic Archipelago, the Beaufort Sea, and the central Arctic basin, while negative influences are found in the western area of the Eastern Siberian Sea and the Laptev Sea. Further, SIT benefits from ensemble SST assimilation. The few available upward-looking sonar observations reveal that the SIT in the Beaufort Sea was significantly improved by assimilating reliable SST observations into light ice areas. Normally, ice temperatures have a stronger impact on SIT than SIC in a heavy ice region. The SIC and SIT are improved synchronously at location B in the Canada Basin as a result of the cross correlations between SST, SIC, and SIT. At locations A and C, only the SIT improved, while there is no significant improvement in SIC, which is partly due to the worsening of the SIC simulation capability at locations A and C.

Because of the weakness of the basin-scale model in the coastal sea and a nonoptimized model configuration in generating ocean mean state, the SST hindcasts without data assimilation are not ideal. However, after assimilating SST observations the SST forecasts are improved. Limited by the computational ability and the large number of model grid points, the experiments are conducted only in summer season in the Northern Hemisphere. Large-scale satellite SIT maps could not be found for the summertime. This fact limits the further assessment of the influence of SST assimilation on SIT. However, the three ULS observation time series in the

Beaufort Sea show that the SIT is also improved, at least regionally and periodically.

Future work will focus on enlarging the ensemble of model states because only four ensemble members will neglect the many possible effects of the SST data assimilation. However, the experiments show that the data assimilation can be applied even with this small ensemble size. This is, perhaps, due to the second-order exact sampling of the initial ensemble, which includes the leading modes of uncertainty, and the fact that the data assimilation is essentially applied as a two-dimensional problem. Further focus will be on optimizing the model configuration and assimilating more ice–ocean variables like SIC, SIT, sea surface level anomaly, and sea surface salinity into the Arctic ice–ocean model system.

Acknowledgments. This work is supported by the BMBF (Federal Ministry of Education and Research, Germany)–SOA (State Oceanic Administration, China) Joint Project (01DO14002), and the National Natural Science Foundation of China (41506224, 41376005, and 41506038).

REFERENCES

Brasseur, G. P., J. T. Kiehl, T. Schneider, C. Granier, X. X. Tie, and D. Hauglustaine, 1998: Past and future changes in global tropospheric ozone: Impact on radiative forcing. *Geophys. Res. Lett.*, **25**, 3807–3810, doi:10.1029/1998GL900013.

——, and Coauthors, 2005: Data assimilation for marine monitoring and prediction: The MERCATOR operational assimilation systems and the MERSEA developments. *Quart. J. Roy. Meteor. Soc.*, **131**, 3561–3582, doi:10.1256/qj.05.142.

Brusdal, K., J. M. Brankart, G. Halberstadt, G. Evensen, P. Brasseur, P. J. van Leeuwen, E. Dombrowsky, and J. Verron, 2003: A demonstration of ensemble-based assimilation methods with a layered OGCM from the perspective of operational ocean forecasting systems. *J. Mar. Syst.*, **40–41**, 253–289, doi:10.1016/S0924-7963(03)00021-6.

Budgell, W. P., 2005: Numerical simulation of ice-ocean variability in the Barents Sea region. *Ocean Dyn.*, **55**, 370–387, doi:10.1007/s10236-005-0008-3.

Candille, G., C. Côté, P. L. Houtekamer, and G. Pellerin, 2007: Verification of an ensemble prediction system against observations. *Mon. Wea. Rev.*, **135**, 2688–2699, doi:10.1175/MWR3414.1.

Di Lorenzo, E., 2003: Seasonal dynamics of the surface circulation in the Southern California Current System. *Deep-Sea Res. II*, **50**, 2371–2388, doi:10.1016/S0967-0645(03)00125-5.

Evensen, G., 1994: Sequential data assimilation with a nonlinear quasi-geostrophic model using Monte Carlo methods to forecast error statistics. *J. Geophys. Res.*, **99**, 10 143–10 162, doi:10.1029/94JC00572.

Giese, B. S., and S. Ray, 2011: El Niño variability in simple ocean data assimilation (SODA), 1871–2008. *J. Geophys. Res.*, **116**, C02024, doi:10.1029/2010JC006695.

Hunke, E. C., 2001: Viscous–plastic sea ice dynamics with the EVP model: Linearization issues. *J. Comput. Phys.*, **170**, 18–38, doi:10.1006/jcph.2001.6710.

——, and J. K. Dukowicz, 1997: An elastic–viscous–plastic model for sea ice dynamics. *J. Phys. Oceanogr.*, **27**, 1849–1868, doi:10.1175/1520-0485(1997)027<1849:AEVPMF>2.0.CO;2.

Jung, T., and Coauthors, 2016: Advancing polar prediction capabilities on daily to seasonal time scales. *Bull. Amer. Meteor. Soc.*, **97**, 1631–1647, doi:10.1175/BAMS-D-14-00246.1.

Kanamitsu, M., 1989: Description of the NMC global data assimilation and forecast system. *Wea. Forecasting*, **4**, 335–342, doi:10.1175/1520-0434(1989)004<0335:DOTNGD>2.0.CO;2.

——, W. Ebisuzaki, J. Woollen, S.-K. Yang, J. J. Hnilo, M. Fiorino, and G. L. Potter, 2002: NCEP–DOE AMIP-II Reanalysis (R-2). *Bull. Amer. Meteor. Soc.*, **83**, 1631–1643, doi:10.1175/BAMS-83-11-1631.

Konig Beatty, C. S., 2012: Arctic landfast sea ice 1953-1998, version 1. National Snow and Ice Data Center, doi:10.7265/N5ZW1HV4, http://nsidc.org/data/g02195.html.

Large, W. G., J. C. McWilliams, and S. C. Doney, 1994: Oceanic vertical mixing: A review and a model with a nonlocal boundary layer parameterization. *Rev. Geophys.*, **32**, 363–403, doi:10.1029/94RG01872.

Lisæter, K. A., J. Rosanova, and G. Evensen, 2003: Assimilation of ice concentration in a coupled ice–ocean model, using the ensemble Kalman filter. *Ocean Dyn.*, **53**, 368–388, doi:10.1007/s10236-003-0049-4.

——, G. Evensen, and S. Laxon, 2007: Assimilating synthetic CryoSat sea ice thickness in a coupled ice-ocean model. *J. Geophys. Res.*, **112**, C07023, doi:10.1029/2006JC003786.

Losa, S. N., S. Danilov, J. Schröter, L. Nerger, S. Massmann, and F. Janssen, 2012: Assimilating NOAA SST data into the BSH operational circulation model for the North and Baltic Seas: Inference about the data. *J. Mar. Syst.*, **105–108**, 152–162, doi:10.1016/j.jmarsys.2012.07.008.

——, ——, ——, T. Janjić, L. Nerger, and F. Janssen, 2014: Assimilating NOAA SST data into BSH operational circulation model for the North and Baltic Seas: Part 2. Sensitivity of the forecast's skill to the prior model error statistics. *J. Mar. Syst.*, **129**, 259–270, doi:10.1016/j.jmarsys.2013.06.011.

Madec, G., P. Delecluse, M. Imbard, and C. Lévy, 1998: OPA 8.1 Ocean General Circulation Model reference manual. Note du Pôle de Modélisation de Institut Pierre-Simon Laplace Note 11, 91 pp.

Marchesiello, P., J. C. McWilliams, and A. Shchepetkin, 2003: Equilibrium structure and dynamics of the California Current System. *J. Phys. Oceanogr.*, **33**, 753–783, doi:10.1175/1520-0485(2003)33<753:ESADOT>2.0.CO;2.

Mellor, G. L., and T. Yamada, 1982: Development of a turbulence closure model for geophysical fluid problems. *Rev. Geophys. Space Phys.*, **20**, 851–875, doi:10.1029/RG020i004p00851.

——, and L. Kantha, 1989: An ice-ocean coupled model. *J. Geophys. Res.*, **94**, 10 937–10 954, doi:10.1029/JC094iC08p10937.

Moore, A. M., H. G. Arango, A. J. Miller, B. D. Cornuelle, E. Di Lorenzo, and D. J. Neilson, 2004: A comprehensive ocean prediction and analysis system based on the tangent linear and adjoint components of a regional ocean model. *Ocean Modell.*, **7**, 227–258, doi:10.1016/j.ocemod.2003.11.001.

Nerger, L., and W. Hiller, 2013: Software for ensemble-based data assimilation systems—Implementation strategies and scalability. *Comput. Geosci.*, **55**, 110–118, doi:10.1016/j.cageo.2012.03.026.

——, S. Danilov, W. Hiller, and J. Schröter, 2006: Using sea level data to constrain a finite-element primitive-equation model with a local SEIK filter. *Ocean Dyn.*, **56**, 634–649, doi:10.1007/s10236-006-0083-0.

Nguyen, A. T., D. Menemenlis, and R. Kwok, 2011: Arctic ice-ocean simulation with optimized model parameters: Approach and assessment. *J. Geophys. Res.*, **116**, C04025, doi:10.1029/2010JC006573.

Overland, J. E., and M. Wang, 2013: When will the Arctic be nearly sea ice free? *Geophys. Res. Lett.*, **40**, 2097–2101, doi:10.1002/grl.50316.

Peterson, B. J., R. M. Holmes, J. W. McClelland, C. J. Vorosmarty, R. B. Lammers, A. I. Shiklomanov, and S. Rahmstorf, 2002: Increasing river discharge to the Arctic Ocean. *Science*, **298**, 2171–2173, doi:10.1126/science.1077445.

Petersen, W., F. Schroeder, and F.-D. Bockelmann, 2011: Ferry-Box—Application of continuous water quality observations along transects in the North Sea. *Ocean Dyn.*, **61**, 1541–1554, doi:10.1007/s10236-011-0445-0.

Pham, D. T., 2001: Stochastic methods for sequential data assimilation in strongly nonlinear systems. *Mon. Wea. Rev.*, **129**, 1194–1207, doi:10.1175/1520-0493(2001)129<1194:SMFSDA>2.0.CO;2.

Rodwell, M. J., S. T. K. Lang, N. B. Ingleby, N. Bormann, E. Hólm, F. Rabier, D. S. Richardson, and M. Yamaguchi, 2016: Reliability in ensemble data assimilation. *Quart. J. Roy. Meteor. Soc.*, **142**, 443–454, doi:10.1002/qj.2663.

Sakov, P., F. Counillon, L. Bertino, K. A. Lisæter, P. R. Oke, and A. Korablev, 2012: TOPAZ4: An ocean-sea ice data assimilation system for the North Atlantic and Arctic. *Ocean Sci.*, **8**, 633–656, doi:10.5194/os-8-633-2012.

Shchepetkin, A. F., and J. C. McWilliams, 2003: A method for computing horizontal pressure-gradient force in an oceanic model with a nonaligned vertical coordinate. *J. Geophys. Res.*, **108**, 3090, doi:10.1029/2001JC001047.

——, and ——, 2005: The Regional Ocean Modeling System: A split-explicit, free-surface, topography following coordinates ocean model. *Ocean Modell.*, **9**, 347–404, doi:10.1016/j.ocemod.2004.08.002.

Song, Y., and D. B. Haidvogel, 1994: A semi-implicit ocean circulation model using a generalized topography-following coordinate system. *J. Comput. Phys.*, **115**, 228–244, doi:10.1006/jcph.1994.1189.

Stanev, E. V., J. Schulz-Stellenfleth, J. Staneva, S. Grayek, J. Seemann, and W. Petersen, 2011: Coastal observing and forecasting system for the German Bight—Estimates of hydrophysical states. *Ocean Sci.*, **7**, 569–583, doi:10.5194/os-7-569-2011.

Tietsche, S., D. Notz, J. Jungclaus, and J. Marotzke, 2013: Assimilation of sea-ice concentration in a global climate model—Physical and statistical aspects. *Ocean Sci.*, **9**, 19–36, doi:10.5194/os-9-19-2013.

Umlauf, L., and H. Burchard, 2003: A generic length-scale equation for geophysical turbulence models. *J. Mar. Res.*, **61**, 235–265, doi:10.1357/002224003322005087.

Wentz, F. J., and T. Meissner, 2000: AMSR ocean algorithm. Algorithm Theoretical Basis Doc., Version 2, Remote Sensing Systems Rep. 121599A-1, 66 pp.

Yang, Q., S. N. Losa, M. Losch, X. Tian-Kunze, L. Nerger, J. Liu, L. Kaleschke, and Z. Zhang, 2014: Assimilating SMOS sea ice thickness into a coupled ice-ocean model using a local SEIK filter. *J. Geophys. Res. Oceans*, **119**, 6680–6692, doi:10.1002/2014JC009963.

——, ——, ——, T. Jung, and L. Nerger, 2015: The role of atmospheric uncertainty in Arctic summer sea ice data assimilation and prediction. *Quart. J. Roy. Meteor. Soc.*, **141**, 2314–2323, doi:10.1002/qj.2523.

Zhang, J., and D. A. Rothrock, 2003: Modeling global sea ice with a thickness and enthalpy distribution model in generalized curvilinear coordinates. *Mon. Wea. Rev.*, **131**, 845–861, doi:10.1175/1520-0493(2003)131<0845:MGSIWA>2.0.CO;2.